Physics of Fluids ARTICLE pubs.aip.org/aip/pof

Relaxation times and dynamic behavior of an optofluidic flow meter in the nanoliter per minute regime

Cite as: Phys. Fluids **36**, 022029 (2024); doi: 10.1063/5.0193599
Submitted: 22 December 2023 · Accepted: 2 February 2024 ·
Published Online: 29 February 2024

View Online Export Citation CrossMark

Nicholas Drachman,[1,a)] Paul N. Patrone,[2] and Gregory A. Cooksey[3,b)]

AFFILIATIONS

[1]Department of Physics, Brown University, Providence, Rhode Island 02912, USA
[2]Information Technology Laboratory, National Institute of Standards and Technology, Gaithersburg, Maryland 20899, USA
[3]Physical Measurement Laboratory, National Institute of Standards and Technology, Gaithersburg, Maryland 20899, USA

[a)]**Also at:** Physical Measurement Laboratory, National Institute of Standards and Technology, Gaithersburg, Maryland 20899, USA.
[b)]**Author to whom correspondence should be addressed:** gregory.cooksey@nist.gov

ABSTRACT

Accuracy and temporal resolution of flow meters are often unacceptable below the microliter per minute scale, limiting their ability to evaluate the real-time performance of many microfluidic devices. For conventional flow meters, this problem arises from uncertainties that depend on physical effects, such as evaporation, whose relative impacts scale inversely with flow rate. More advanced techniques that can measure nanoliter per minute flows are often not dynamic and require specialized equipment. Herein, we report on new experimental and theoretical results that overcome both limitations using an optofluidic flow meter. Previously, we showed that this device can measure flow rates as low as 1 nl/min with roughly 5% relative uncertainty by leveraging the photobleaching rate of a fluorescent dye. We now extend that work by determining the flow meter's relaxation time over a wide range of flow rates and incident irradiances. Using a simplified analytical model, we deduce that this time constant arises from the interplay between the photobleaching rate and transit time of the dye through the optical interrogation region. This motivates us to consider a more general model of the device, which, surprisingly, implies that all time constants are related by a simple scaling relationship depending only on the flow rate and optical irradiance. We experimentally validate this relationship to within 5% uncertainty down to 1 nl/min. Additionally, we measure a relaxation time of the flow meter on the order of 100 ms for 1 nl/min flows, demonstrating the ability to make dynamic measurements of small flows with unprecedented accuracy.

Published by AIP Publishing. https://doi.org/10.1063/5.0193599

29 February 2024 14:37:48

I. INTRODUCTION

An increasing number of micro- and nano-fluidic applications require the control of fluid flows in the nanoliter per minute regime. These include drug infusion,[1–3] nano-electrospray ionization (nanoESI),[4,5] and high pressure liquid chromatography (HPLC),[6] among others. Accurate measurement of flow rates is critical to understanding and improving the performance of these technologies. In addition, many nanoflow applications are sensitive to small fluctuations in flows. In nanoESI, for example, small changes in flow can cause significant variation in an ion's ionization response, which propagates to downstream uncertainties.[4] In HPLC, pumps operate on short cycles (≈1 Hz) whose fluctuations can blur chromatography peaks.[7] In infusion therapy, drug dosing is determined via flow rate measurements, which must be well controlled to ensure the correct amount of medicine is delivered, an issue of particular importance for neonates.[8,9]

In this context, a key problem limiting the advancement of such microfluidic systems is an inability to easily quantify and control uncertainty in dynamic flows. Several groups have recently begun developing traceable calibration systems in an attempt to measure fast changing flow rates down to 5 nl/min.[1,3,8,10–13] These measurements are generally short duration (limited by microscopic observations of a moving interface) and cannot be tracked continuously.[14–16] They may also suffer from uncertainty associated with interfacial dynamics at the flow channel walls.[10] Gravimetric methods are the gold-standard for traceable microflow measurements, but they cannot measure dynamic nanoflows due to the need for long integration times and uncertainties associated with evaporation and small system geometries.[17,18] Microparticle imaging velocimetry is perhaps the most accurate of the more widely used flow metrology techniques in the range of single nanoliter per minute flow rates, but it requires a detailed knowledge of the

system geometry, a powerful fluorescence microscope, associated computational demands, and long observation times at lower flows.[19,20] For these reasons, a new metrology technique capable of measuring fast-changing flows in the nanoliter per minute regime is needed.

Previously, we reported an optofluidic flow meter that can measure flows down to 1 nl/min with less than 5% uncertainty.[21–24] This instrument works by measuring the photobleaching of a fluorescent dye in a fluid as it traverses a small interrogation region, which is defined by an excitation beam projected through a waveguide onto a specific region of a microfluidic channel. Figure 1(a) shows a characteristic device. When fluid containing a fluorescent dye flows through the interrogation region, it is irradiated by laser light coming through the excitation waveguide. The resulting fluorescence is collected by the upstream and downstream fluorescence waveguides and measured by photodetectors (not shown). A separate photodetector measures the excitation light transmitted through the transmission waveguide to track fluctuations in the laser power. Notably, fluorophores in water photobleach after roughly (10^4–10^6) absorption and emission cycles.[25–28] At lower flow rates, each dye molecule will spend more time traversing the excitation beam, thus being exposed to more photons and increasing its probability of photobleaching. In Refs. 21–24, we showed that this observation implies that the measured steady-state fluorescence efficiency, I/P, scales with the dosage, $\xi = \frac{f(P)}{Q}$, where I is the measured fluorescence intensity, P is the laser power, Q is the flow rate, and f is a fixed, experimentally determined function of P.[22,23] The flow meter is calibrated by obtaining the one-to-one master curve that relates every value of I/P to a unique ξ. This is done by measuring the steady state fluorescence efficiency over a range of known laser powers and flow rates (see Sec. III B for description of how flow rates are determined during calibration). Given this calibration curve, one can determine unknown flow rates from the measured I/P at some known value of P.

In this work, we study the dynamics of the optofluidic flow meter to determine the fluorescence intensity following a perturbation in the dosage. We start by considering a simplified analytical model that provides intuition about how the dynamics of the fluorescence signal depend on the flow rate and laser power. The practical limitations of this model motivate us to revisit the full theory from Ref. 22, from which we derive a simple scaling relationship that relates the relaxation time, λ, at different flow rates. Importantly, this scaling relationship generalizes the method of calibrating the flow meter for measuring steady-state flow rates described earlier. In particular, by using transient data that is already collected during the steady-state calibration process, λ can be determined for any combination of flow rate and laser power.

The primary objective of this work is to establish the basic processes that determine the dynamic response of optofluidic flow measurements. Additionally, we aim to demonstrate that an optofluidic flow meter can reliably measure real-time flows at the nanoliter per minute scale.

II. THEORY

A fully time-dependent model of the optofluidic flow meter is difficult to solve analytically. However, a simplified version can be used to identify the basic physical effects that determine both the steady state and dynamics of the measured fluorescence intensity. Informally speaking, an initial condition in which the laser is off and the dye concentration is constant represents a "worst-case" scenario at low flow rates, i.e., one that is "furthest" from the steady state. Thus, we restrict our analysis to the situation in which the flow rate is time independent and the laser is turned on at $t = 0$.

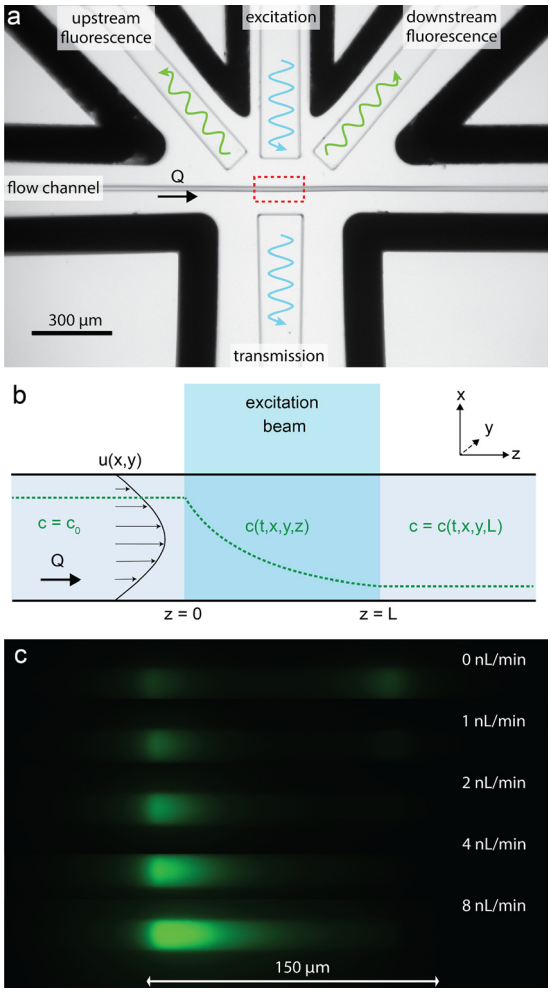

FIG. 1. (a) Bright field image of the flow meter's optical interrogation region. Fluid flows from left to right through the interrogation region in the flow channel, where it interacts with 488 nm laser light. Emitted fluorescence is collected by the upstream and downstream fluorescence waveguides, and transmitted light is collected by the lower waveguide. Channels filled with black PDMS are used to block light leakage between waveguides. The dashed red box surrounds the region of the flow channel being interrogated. (b) Diagram illustrating the physical model we use to describe the dynamics of the measurement process. The dashed green curve represents the concentration of unbleached fluorophores within the channel, $c(t, x, y, z)$, and the solid black curve represents the Poiseuille flow velocity profile of the fluid, $u(x, y)$. (c) Fluorescence microscopy images of the interrogation region at various flow rates at a constant laser power of 12.5 mW. The amount of photobleaching decreases with increasing flow rate, enabling the quantification of flow rate through a fluorescence measurement.

Figure 1(b) shows a sketch of the model we use to describe the measurement device, which indicates the Poiseuille flow velocity profile, $u(x, y)$, and the time-dependent distribution of unbleached fluorophores, $c(t, x, y, z)$. At $t = 0$, the concentration of unbleached fluorophores everywhere in the channel is $c = c_0$. At this instant, the

29 February 2024 14:37:48

laser is turned on and fluorophores in the interrogation region between $z=0$ and $z=L$ are irradiated and begin to bleach. At $z=L$, the fluorophores exit the excitation beam and experience no further bleaching, so $c(z>L)\equiv c(z=L)$. As $t\to\infty$, the system reaches a steady state that is spatially varying in the interrogation region. It is this steady state condition that is used to measure the flow rate.[21,22,24] Figure 1(c) shows fluorescence microscopy images of the interrogation region at steady state for flow rates ranging from 0 to 8 nl/min and a constant laser power of 12.5 mW (all laser powers quoted in this work represent the nominal power emitted by the laser). Faster flows generate a stronger fluorescence signal, and at zero flow, a dim signal is seen on both sides of the interrogation region, as unbleached fluorophores diffuse in from both sides. Here, we seek to quantify the relaxation time, λ, that defines the time to approach this steady state following a perturbation.

A. Notation

Table I summarizes the definitions of key terms and notation for convenience.

B. Simplified linear model

The simplified linear partial differential equation (PDE) governing the photobleaching process is

$$\frac{\partial c}{\partial t}=D\nabla^2 c-u(x,y)Q\frac{\partial c}{\partial z}-f(P)\phi\Theta(z)c, \tag{1}$$

where c is the concentration of unbleached fluorophores, D is the diffusion coefficient, $u(x,y)$ is a function representing the Poiseuille flow profile with units m^{-2}, Q is the volumetric flow rate, $f(P)$ is a monotonically increasing function of the laser power, P, ϕ is the photobleaching efficiency, and Θ is the Heaviside step function.[22] The three terms on the right-hand side of Eq. (1) account for diffusion, advection, and photobleaching, respectively. We assume the Peclet number is high for the purposes of this analysis (see Appendix B for a calculation of the Peclet number), and drop the diffusion term from Eq. (1), yielding

$$\frac{\partial c}{\partial t}=-u(x,y)Q\frac{\partial c}{\partial z}-f(P)\phi\Theta(z)c. \tag{2}$$

Equation (2) can be solved analytically by shifting to a coordinate system that is co-moving with the flow (see Appendix A for a detailed derivation). The solution is given by

TABLE I Definitions of key symbols.

Variable	Definition
P	Laser power
Q	Volumetric flow rate
ξ	Dosage, i.e., amount of light absorbed during transit
c	Concentration of *unbleached* fluorophore
c_0	Total fluorophore concentration
λ	Relaxation time constant
$\Theta(z)$	Heaviside step function

$$c(t,x,y,z)=\begin{cases}c_0\exp\left(-\dfrac{\xi\phi z}{u(x,y)}\right) & \text{if } z<u(x,y)Qt,\\ c_0\exp(-\xi\phi Qt) & \text{if } z>u(x,y)Qt,\end{cases} \tag{3}$$

where $u(x,y)Qt$ is the distance into the laser beam that the fluorophores starting at $z=0$, $t=0$ have penetrated along the particular streamline parameterized by the position (x,y). The first case in Eq. (3) describes the contribution fluorophores that started outside of the interrogation region ($z<0$) when the laser was turned on ($t=0$). This term is z-dependent but not explicitly t-dependent because the probability of these fluorophores bleaching does not depend on how long it has been since the laser was turned on, but rather how far they have penetrated into the interrogation region. The second case in Eq. (3) describes the contribution of fluorophores that started inside the interrogation region at $t=0$. This term is t-dependent but not z-dependent because, while these fluorophores are still in the interrogation region, the probability of bleaching depends only on how much time has passed since the laser was turned on.

To find the measured fluorescence intensity, we multiply the excitation power, P, by the total number of unbleached fluorophores in the channel and by the fluorescence efficiency, Φ, which includes both the fluorescence quantum yield and optical factors related to fluorescence collection,

$$I(t)=P\Phi\int_V c(t,x,y,z)\,dx\,dy\,dz. \tag{4}$$

Because diffusion is assumed to be negligible, we may treat each streamline independently. Equation (4) can be evaluated for two separate regimes, representing the times before all fluorophores that were within the interrogation region at $t=0$ have exited the region, and the times after those initial fluorophores have exited the interrogation region. When $0<u(x,y)Qt<L$, we need to consider both terms in Eq. (3),

$$I(t,x,y)=P\Phi c_0\left[\int_0^{uQt}\exp\left(-\frac{\xi\phi z}{u}\right)dz+\int_{uQt}^{L}\exp(-\xi\phi Qt)\,dz\right]. \tag{5}$$

When $u(x,y)Qt>L$, we only need to consider the first term in (3),

$$I(t,x,y)=P\Phi c_0\int_0^{L}\exp\left(-\frac{\xi\phi z}{u}\right)dz. \tag{6}$$

Evaluating these integrals yields an expression for the fluorescence intensity measured from each streamline in the channel,

$$I(t,x,y)=P\Phi c_0\begin{cases}\left(L-uQt-\dfrac{u}{\xi\phi}\right)e^{-\xi\phi Qt}+\dfrac{u}{\xi\phi} & \text{if } t<\dfrac{L}{uQ},\\ -\dfrac{u}{\xi\phi}\exp\left(-\dfrac{\xi\phi L}{u}\right)+\dfrac{u}{\xi\phi} & \text{if } t>\dfrac{L}{uQ},\end{cases} \tag{7}$$

where we have used $u\equiv u(x,y)$ for compactness.

In light of Eq. (7), a few comments are in order:

1. The dynamics of the system depend on the competition between two timescales, the advection time $\frac{L}{uQ}$ and the bleaching time $\frac{1}{\xi\phi Q}=\frac{1}{f(P)\phi}$.
2. Advection leads to the piece-wise structure in Eq. (7). The quantity $t=\frac{L}{uQ}$ represents the time it takes for a fluorophore in a

29 February 2024 14:37:48

given streamline to cross the full length of the interrogation region. For a fixed pair (x, y), this is the maximum time to steady state, since all fluorophores that were in the interrogation region at $t = 0$ have exited it.

3. The first case in Eq. (7) is the transient fluorescence intensity of particles that were already in the interrogation region $(0 < z < L)$ when the laser was turned on at $t = 0$, while the second case corresponds to the steady state fluorescence intensity of fluorophores that were upstream of the interrogation region at $t = 0$.
4. The exponential term in the first case does not depend on flow rate, so the initial rate at which fluorescence decays depends only on P and ϕ. This can be shown more explicitly by taking the derivative of Eq. (7) and then taking the limit as $t \to 0$.
5. The exponential term in the second case is the ratio of the advection time to the bleaching time. So the steady-state fluorescence intensity depends both on the laser power and the flow rate.

C. General scaling relationship

A key advantage of the optofluidic flow meter compared to other nanoflow metrology techniques is that no detailed knowledge of the photophysics or system geometry [i.e., Φ, ϕ, and $u(x, y)$] are necessary to make an accurate measurement.[21,22] However, without this knowledge, a complete time-dependent model of the flow meter cannot be made explicit. For this reason, we seek to generalize the scaling relationship of Ref. 22 [Eq. (25) therein].

Consider therefore the general PDE describing the photobleaching process for an arbitrary laser profile,

$$\frac{\partial c}{\partial t} = u(x,y)Q\frac{\partial c}{\partial z} - f(P)B(c,x,y,z), \tag{8}$$

where $B(c, x, y, z)$ is a potentially non-linear, non-local function of concentration and position; see Patrone *et al.* for a justification of this model and list of assumptions on B.[23] Rescaling Eq. (8) in terms of $\tau = Qt$ gives

$$\frac{\partial c}{\partial \tau} = u(x,y)\frac{\partial c}{\partial z} - \xi B(c,x,y,z). \tag{9}$$

This rescaled PDE depends explicitly on the dosage but is invariant with respect to the flow rate, Q. If we assume that the laser power and profile are time-independent, the measured fluorescence intensity is given by

$$I(t) = P\int_V F[c(r, Qt;\xi), r]d^3r, \tag{10}$$

where $F[c, r]$ is a potentially nonlinear function representing the amount of fluorescence light collected from position r for concentration $c(r, Qt; \xi)$. Note that for a fixed position r, F is a monotonically increasing function of concentration. See Refs. 22 and 23 for further discussion of F. Equation (10) states that the fluorescence intensity is dependent on t only through the flow-scaled time Qt, and when written in terms of the flow-scaled time, Q is no longer a parameter,

$$I(t; Q, \xi) \equiv I(Qt; \xi). \tag{11}$$

Therefore, if the dosage is fixed at some value $\xi = \xi_0$, but the flow rate changes from Q_0 to Q_1, $I(Q_1 t; \xi_0)$ is just a rescaled version of $I(Q_0 t; \xi_0)$. If λ is the relaxation time of the flow meter at some reference flow rate, Q_0, and dosage, ξ_0, Eq. (11) implies the scaling relationship

$$\lambda(Q_1; \xi_0) = \frac{Q_0}{Q_1}\lambda(Q_0; \xi_0). \tag{12}$$

Equation (12) is a surprising and useful result. It tells us that if the dynamics of the flow meter are known for some value of Q and ξ, they are known for every Q as long as ξ is held fixed. It allows one to determine the relaxation time of the flow meter at *any* Q and P, just by measuring the relaxation time at a *single* Q value, and sweeping over laser powers to sample a wide dosage range. Stated differently, the relaxation time λ is nominally a function of two variables (Q and ξ) but can be reduced to a function of only ξ by rescaling time. Note that, like the analysis of steady-state performance of the flow meter, this conclusion does not require detailed knowledge of the photophysics or channel geometry.[21,22]

III. METHODS

A. Flow meter fabrication

The flow meter consists of a microfluidic network that is made out of poly(dimethylsiloxane) (PDMS) and contains microchannels for fluids, waveguides, and light-blocking materials. The flow channel is 100 μm deep and varies from 15 μm wide in the interrogation region [shown in Fig. 1(a)] to 100 μm wide far from the interrogation region. The flow channel also contains two additional 5 cm long segments with $40 \times 100\ \mu m^2$ cross section to decrease the fluidic conductance of the chip, the measurement of which is described below.

The device was realized in two layers, a top layer that contained the flow channel, optical fiber inlets, waveguides, light blocking channels, and debris traps and a bottom layer that contained additional light-blocking channels and relief channels that facilitate fiber insertion. A full description of the flow meter fabrication can be found in Ref. 21. Briefly, a mold with features defined by an epoxy-based negative photoresist on a silicon wafer was made by conventional photolithography techniques. The top and bottom PDMS layers were then cast from the mold using standard soft lithography techniques. Devices were thermally cured at 70 °C for 4 h, razor cut, and adapted for fluidic input by coring inlet ports with a 1.0 mm micropunch through the top layer. The top layer was then stamped on a thin layer of PDMS crosslinker followed by crude contact alignment to the bottom layer. The top layer was then slid over the bottom layer while observing registration of alignment markers in each layer under an optical microscope (5× objective). Another thermal curing process followed alignment to bond the layers together. The light-blocking channels were then filled with black PDMS and thermally cured. Waveguide channels were filled with optical adhesive (refractive index of approximately 1.56) under vacuum followed by insertion of cleaved optical fibers. Waveguides were polymerized around fibers using an ultraviolet light shone over the device for 1 h (365 nm, 100 W bulb) and further cured by connecting optical fibers to a 375 nm laser at 70 mW for 5 min. A 200 mW, 488 nm laser was used as source for excitation light to the interrogation regions. Light was coupled from the laser to the device through a multimode optical fiber [0.1 numerical aperture (NA), 105 μm core] inserted into on-chip waveguides.

29 February 2024 14:37:48

Light from the interrogation region was carried from the waveguides to photodetectors by multimode optical fibers with larger NA (0.22 NA, 105 μm core). For the upstream and downstream fluorescence, the photodetectors were photomultiplier tubes preceded by fluorescence emission filters (500–540 nm bandpass), and for the transmitted light, the photodetector was a silicon photodiode connected to a power meter (1 W maximum power). Fluidic connections were made with blunted 21-gauge syringe needles with adapters to rigid tubing. All fluorescence measurements presented here were made using 10 μmol/L of fluorescein isothiocyanate-dextran (FITC-dextran) (70 kD) in borate buffer (50 mmol/L, pH 8.5) as the working fluid.

B. Flow meter characterization

A single flow meter was used to make all measurements presented in this paper. The fluidic conductance of the flow meter was measured by the procedure described in Ref. 21. Flow was driven by hydrostatic pressure of a liquid reservoir mounted on a 1 m tall, vertical motorized stage with 2 μm position accuracy. Utilizing the vertical stage as a flow controller involves determining the relationship between Q and Δh, the height of the liquid reservoir above zero flow. We determine the height of zero flow by watching for a symmetric bleaching in the interrogation region while adjusting the height of the vertical stage [see Fig. 1(c)].[21] We set this position close to 50 mm above the bottom of the vertical stage by adjusting the height of the waste collection reservoir. Next, we measured Q at maximum pressure ($\approx 9.316 \times 10^3$ Pa or 950 mmH_2O) using a calibrated thermal flow meter (5% uncertainty at 1 μl/min) and determined the conductance of the system using

$$\sigma = \frac{Q}{\Delta p}, \tag{13}$$

where Δp is the applied pressure (not to be confused with laser power, P) and is equivalent to $\rho g \Delta h$, where ρ the density of water, and g is the acceleration due to gravity. The conductance of the flow meter was measured to be 0.128 nl/(min Pa) $\pm$ 0.006 nl/(min Pa). All flow rates stated in this paper were calculated from Eq. (13), given the measured conductance value and precise knowledge of Δp from Δh.

To measure the dynamics and steady state behavior of the flow meter, the fluorescence and transmitted intensities were recorded at a variety of flow rates and laser powers for at least 20 s following the laser being turned on. The fluorescence and transmitted signals were recorded at a sample rate of 2.5 kHz using a high-speed data acquisition card (DAQ).

C. Data analysis

Equation (12) does not require a particular method to define the relaxation time constant. As a practical demonstration, we determined relaxation time constants by finding the time needed for the normalized fluorescence intensity to decay to 1/e of the difference between its maximum value following the laser being turned on and its steady-state value as $t \to \infty$ [see Fig. 5(a)]. The process for normalization was as follows: (1) The upstream and downstream fluorescence values were summed to obtain the total measured fluorescence, I_{tot}. (2) The minimum value of I_{tot} (i.e., the steady-state value) was found and subtracted from I_{tot} to get ΔI, which is the difference between the fluorescence intensity and the steady-state fluorescence intensity. (3) Finally, ΔI was divided by its maximum value to obtain ΔI_{norm},

$$\Delta I_{norm}(t) = \frac{I_{tot}(t) - \min_t[I_{tot}(t)]}{\max_t\{I_{tot}(t) - \min_t[I_{tot}(t)]\}}. \tag{14}$$

We then found the relaxation time constant, λ, such that

$$\Delta I_{norm}(t = \lambda) = \frac{1}{e}. \tag{15}$$

D. Uncertainty calculations

All flow rates were calculated using Eq. (13), so the uncertainty in the flow rate is dependent on the uncertainties in the conductance and the reservoir height, respectively. The conductance itself is measured by determining the flow rate at some high stage height, h, using a separate, calibrated thermal flow meter, as well as determining the height where the flow rate is 0, h_0. The measurement uncertainty of the thermal flow meter is 5%. Meanwhile, the uncertainty on h_0 is estimated to be about 10 μm, the change in height required to distinguish positive from negative bias in the flow direction [see Fig. 1(c)]. The vertical stage itself has an absolute uncertainty of just 2 μm. Therefore, the uncertainty in both the conductance and all flow rates quoted herein is expected to be dominated by the uncertainty of the thermal flow meter, or about 5%.

All dosages are calculated using Eq. (18), so the uncertainty in dosage depends on the uncertainties in the flow rate and power. By propagation of uncertainty,[29] we find

$$\varepsilon_\xi = \sqrt{\left(\frac{\gamma P^{\gamma-1}}{Q}\right)^2 \varepsilon_P^2 + \left(-\frac{P^\gamma}{Q^2}\right)^2 \varepsilon_Q^2}, \tag{16}$$

where ε_ξ, ε_P, and ε_Q are the uncertainties in dosage, power, and flow rate, respectively. The uncertainty in the laser power is expected to be no larger than 1% based on manufacturer specifications and our experience. As an example, using the lowest flow rate curve in Fig. 3, where $Q = 2$ nl/min and $P = 20$ mW. The uncertainty in the dosage is given by

$$\varepsilon_\xi = \sqrt{\left(\frac{1.3(20)^{0.3}}{2}\right)^2 0.2^2 + \left(-\frac{20^{1.3}}{2^2}\right)^2 0.1^2} = 1.27\,\text{mW} \cdot \text{min/nl}. \tag{17}$$

The measurement uncertainty in the time constants presented in Fig. 4 are primarily due to the finite rise time of the laser. This rise time is about 5 ms, and this variation in laser power cannot be easily deconvoluted from the fluorescence intensity data, so we take the absolute measurement uncertainty of the flow meter's time constants to be 5 ms. In Fig. 4, the measurement uncertainties are also scaled by $\frac{Q}{Q_0}$, where we choose $Q_0 = 1$ nl/min.

IV. RESULTS AND DISCUSSION

A. Dynamic response of flow meter

Figure 2 shows the dynamic response of the flow meter over a range of flow rates and powers. In particular, the plot shows the total fluorescence intensity (upstream + downstream) divided by the total fluorescence intensity at $t = 0$, the time at which the laser is turned on and the fluorescence intensity should be at its maximum value.

29 February 2024 14:37:48

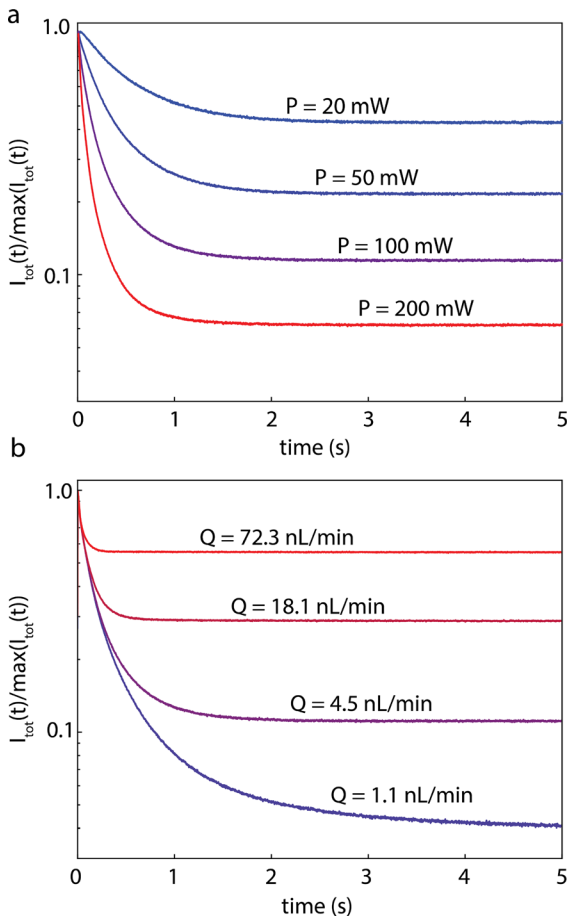

FIG. 2. Plots of the normalized total fluorescence intensity (upstream plus downstream) vs time with 70 kD FITC-dextran. (a) Q fixed at 4.5 nl/min with P ranging from 20 to 200 mW (blue to red). (b) P fixed at 100 mW with Q ranging from 1.1 to 72.3 nl/min (blue to red).

In Fig. 2(a), the flow rate is held constant at 4.5 nl/min, while the power is varied from 20 to 200 mW. Each curve shows an initial decrease in fluorescence intensity, which then reaches a steady-state value. The time to reach steady-state is roughly constant for each power, around 1.5 s, while the rate at which the fluorescence intensity approaches steady-state (i.e., the initial slope of the curve) increases with increasing power. This matches the behavior predicted by Eq. (7), in which the advection time averaged over all streamlines ($\frac{L}{\bar{u}Q}$) approximately characterizes the time to reach steady-state and is independent of P (Sec. II B, comment 2). The steady-state values in Fig. 2(a) also appear to decrease exponentially with increasing power, another feature predicted by Eq. (7) (the P out front in the second case cancels with the ξ's in the denominator of both terms, leaving only the ξ in the exponent).

In Fig. 2(b), the power is held constant at 100 mW, and the flow rate is varied from 1.1 to 72.3 nl/min. Here, the time to reach steady-state increases with decreasing flow rate, while the initial slope is constant with P. This behavior is also predicted by Eq. (7), in which the rate at which the fluorescence intensity approaches its steady-state value at small t depends only on P but not on Q (Sec. II B, comment 4). At larger t, the second term of the first case in Eq. (7) introduces a flow rate dependence in the dynamics, which can be seen in Fig. 2(b) as the curves begin to diverge from their initial slope. These results validate the qualitative dependencies on Q and P predicted by Eq. (7).

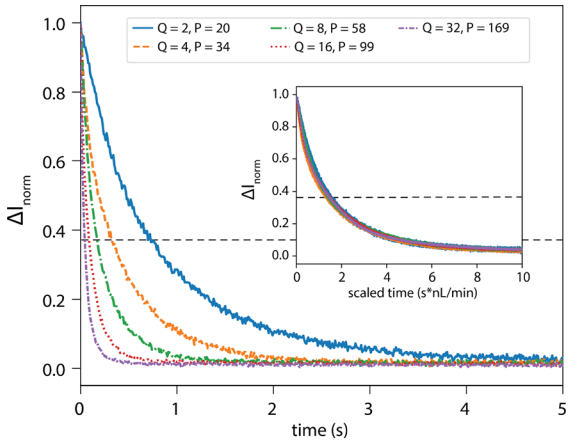

FIG. 3. Normalized fluorescence vs time curves for five different flow rates at constant dosage. Inset demonstrates the scaling relationship given in Eq. (12), each curve is scaled in time according to $t \rightarrow Qt$. The dashed lines represent $\Delta I_{norm} = 1/e$. The units of the flow rate and power are nl/min and mW, respectively, and the relative uncertainties are 1% and 5%, respectively. Data were collected at $\xi = (24.5 \pm 1.3)$ mW · min/nl.

B. Scaling relationship validation

While the results above validate our physical model of the flow meter's dynamics given in Eq. (7), it is the scaling relationship given in Eq. (12) that will be most useful to users of an optofluidic flow meter. To validate this scaling relationship, we measured the dynamic response of the flow meter over a wide dosage range by varying flow rates and laser powers. We show that the relationship holds over three decades of dosage, quantify the measurement uncertainty in λ, and discuss the limitations of our experimental setup in measuring λ at low dosage.

1. Scale invariance of I_{norm} vs time curves at fixed dosage

Figure 3 shows the normalized change in fluorescence intensity (ΔI_{norm}) vs time at five flow rates ranging from 2 to 32 nl/min but with the dosage held fixed at 24.5 mW · min/nl by corresponding changes in the laser power. To maintain a constant dosage across the five measurements, the necessary power was calculated using the relationship

$$\xi = \frac{P^{\gamma}}{Q}, \tag{18}$$

where $\gamma = 1.3$ is an empirically determined power factor.[30] This approximate value of γ was previously found to produce the best calibration curve relating steady-state fluorescence intensity to flow rate.[24] In the inset of the figure, the same fluorescence intensity curves have been replotted as a function of the flow-scaled time, $\tau = tQ$. This causes the curves to collapse to a single curve, demonstrating their scale invariance and validating the scaling relationship given in Eq. (12).

29 February 2024 14:37:48

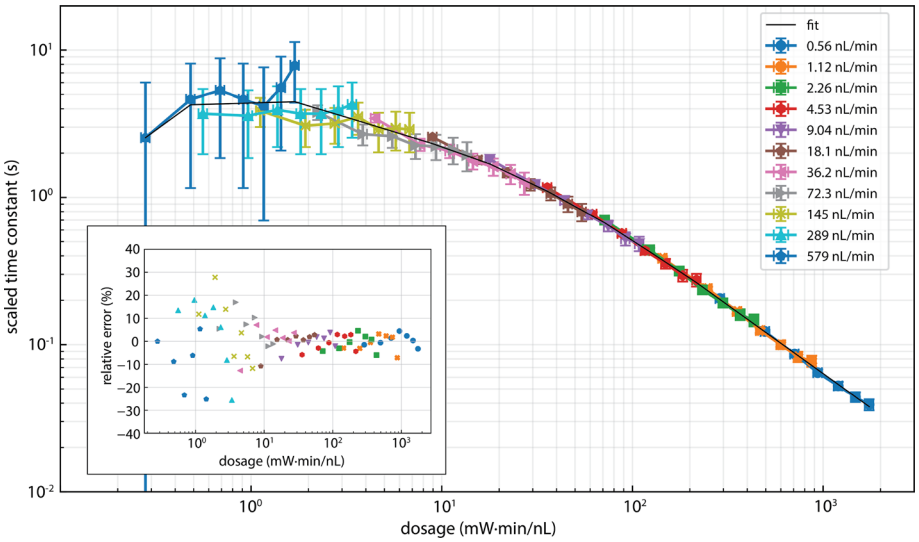

FIG. 4. Scaled time constants ($\tilde{\lambda} = \frac{Q}{Q_0}\lambda$) vs dosage for a wide range of flow rates. The scaled time constants all fall on a single master curve, which relates the relaxation time of the flow meter at any flow rate and dosage to the relaxation time at any other flow rate and dosage. The best fit curve obtained by convex optimization is shown as a solid black curve. The inset shows the relative error of each data point. Relative errors are the differences between the measured time constant and the time constant predicted by the calibration curve divided by the latter. The error bars in the x and y directions represent the individual uncertainties in the dosage and scaled time constants for each measurement, respectively.

2. Master curve

In addition to predicting the data collapse illustrated in Fig. 3, Eq. (12) also implies that the flow-scaled time constants should depend only on the dosage. Therefore, if we measure the flow-scaled constants over a wide range of dosages, they should fall on a single master curve. Figure 4 shows this master curve, where the scaled time constant ($\tilde{\lambda} = \frac{Q}{Q_0}\lambda$, where we choose $Q_0 = 1$ nl/min) is plotted as a function of dosage for dynamics measurements taken over a wide range of flow rates and powers. The powers used were 20, 50, 75, 100, 125, 150, 175, and 200 mW. A power factor of $\gamma = 1.3$ was again used to calculate the dosage according to Eq. (18). The scaling relationship appears to hold remarkably well across three orders of magnitude in dosage.

We have shown that the master curve can be produced by a single-point calibration. Measuring the relaxation time constant at a single flow rate over a wide range of laser powers allows one to scan over dosage and effectively sample the full parameter space. This is analogous to the master calibration curve for flow rate shown previously by Cooksey and Patrone *et al.*, which can be produced by fixing Q and measuring the steady-state fluorescence intensity over a wide range of P values.[21,22] In fact, master calibration curves for *both* the steady state fluorescence intensity *and* the relaxation time can be generated from the same procedure previously used to calibrate the flow meter, since the characteristic relaxation times are on the order of seconds.

In practice, one can use the master curve from Fig. 4 to estimate the limits of measuring dynamics of flow at some target flow rate given a fixed laser power. For example, if one wanted to use the optofluidic flow meter to quantify fluctuations from a pump generating a flow of around 10 nl/min using a laser power of 100 mW ($\xi \approx 40$ mW · min/nl), we see from Fig. 4 that this corresponds to a scaled time constant of 1 s, or 0.1 s at 10 nl/min. So in this example, fluctuations slower than about 10 Hz should be measurable by the optofluidic flow meter. If one desired to measure faster fluctuations at this flow rate, the laser power could be increased, shifting further to the right on the master curve.

3. Uncertainty and limitations on the measurement of λ

The inset of Fig. 4 shows the relative error between the measured time constants and the predicted time constants from the master curve. The calibration curve, shown in solid black in the main figure, was obtained by fitting the data using a convex optimization algorithm.[22] At high dosage ($\gtrsim$10 mW · min/nl), the relative error tends to be around $\pm$5% or less. However, the error becomes large at low dosages. These high relative errors are not due to any known breakdown of the theory at low dosage, but rather the limitations in our experimental setup, namely the data acquisition rate. These limitations make it difficult to accurately measure the dynamics of the fluorescence signal at flow rates >100 nl/min, when the advection time becomes very short. As noted in our previous manuscript,[21] these performance limits are not absolute, and can be adjusted for particular applications by changing the cross-sectional area of the optical interrogation region.

Figure 5 demonstrates the limitations of our experiment with respect to determining the time constant of the flow meter at low dosage. The figure shows the normalized total fluorescence intensity ($\frac{I_{tot}}{\max(I_{tot})}$) and the normalized transmission intensity ($\frac{I_{trans}}{\max(I_{trans})}$) for two different measurements. Figure 5(a) shows the data for a moderately high dosage [$\xi = (44 \pm 2.3)$ mW · min/nl], and panel Fig. 5(b) shows the data for a low dosage [$\xi = (0.14 \pm 0.01)$ mW · min/nl]. In the high dosage case, the decay toward steady state is clear and occurs over a timescale that is long compared to the sampling rate and the rise time of the laser. The initial oscillations in laser power are also small relative to the change in fluorescence intensity. In the low dosage case, the decay toward steady-state is hardly visible as the steady-state value is so close to the maximum value. It occurs on a timescale that is similar to the sampling rate and slow compared to the rise time of the laser. In addition, the steady-state value closely tracks small oscillations in the laser power. These facts all conspire to make the time constant more difficult to measure at low dosage or high flow, resulting in larger relative errors as seen in the inset of Fig. 4.

It should be noted that we have defined λ in terms of the measured fluorescence efficiency, but the fluorescence efficiency is

29 February 2024 14:37:48

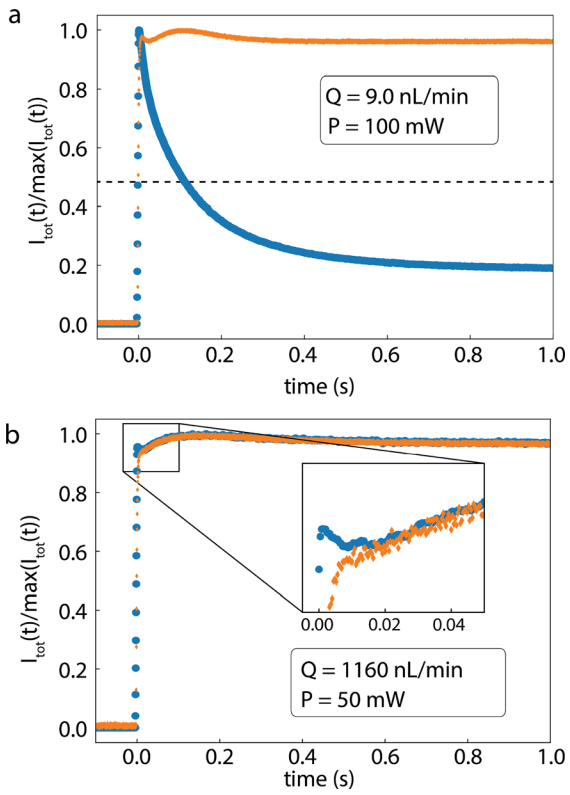

FIG. 5. Comparison of raw fluorescence intensity data at high dosage (a) and low dosage (b). The large blue dots show normalized fluorescence intensity data $(\frac{I_{tot}}{\max(I_{tot})})$, and the small orange diamonds show normalized laser transmission intensity. (a) $\xi = (44 \pm 2.3)$ mW · min/nl. (b) $\xi = (0.14 \pm 0.01)$ mW · min/nl. The black dashed line in (a) shows the $1/e$ threshold, which defines the relaxation time constant.

nonlinearly related to the flow rate. So the uncertainty in the flow rate at $t = \lambda$ following a perturbation is not necessarily $1/e$.

V. CONCLUSION

We have developed an optofluidic flow meter that is capable of measuring ultralow flow rates to 1 nl/min and below. The novelty of this work lies in the use of a basic physics approach to characterize the dynamic properties of an ultralow flow metrology technique, as well as the demonstration that an optofluidic flow meter can measure 1 nl/min flows with a relaxation time of around 100 ms. We derived a general scaling relationship relating the relaxation time of the flow meter at one flow rate to the relaxation time at any other flow rate through dosage. This scaling relationship allows us to generate a master calibration curve that captures the dynamics of the flow meter response for a broad range of dosages, covering almost three orders of magnitude in flow rates. Effectively, this relationship enables one to estimate the rates of change they could expect to measure at a given flow rate and laser power. Similarly, one can use the relationship to estimate the uncertainty in a flow measurement after a certain amount of time (e.g., from an expected relaxation time constant). Overall, these findings extend the measurement capabilities of our previous work relating the steady-state fluorescence efficiency to the flow rate, demonstrating that both the steady-state and dynamics of the flow meter can be fully characterized by scanning a broad range of irradiances at a single calibrated flow rate.

ACKNOWLEDGMENTS

We acknowledge Jalal Sadeghi and Matthew DiSalvo for fabricating the silicon master molds, which was conducted at the NIST Center for Nanoscale Science and Technology. N.D. acknowledges support of a Graduate Fellowship for STEM Diversity from NIST and helpful discussions with Derek Stein. G. A.C. and P.N.P. acknowledge U.S. patent 15/967,966 related to this publication. We thank Anthony Kearsley for helpful discussions. This work was partially supported through the NIST on a Chip Program, https://www.nist.gov/noac.

AUTHOR DECLARATIONS

Conflict of Interest

Yes, the US government has a patent on the technology presented from which we can receive royalties.

Author Contributions

Nicholas Drachman: Conceptualization (supporting); Data curation (lead); Formal analysis (equal); Investigation (lead); Methodology (equal); Software (lead); Validation (equal); Visualization (lead); Writing – original draft (lead); Writing – review & editing (lead). **Paul N. Patrone:** Conceptualization (equal); Formal analysis (equal); Funding acquisition (supporting); Investigation (supporting); Methodology (equal); Supervision (supporting); Validation (equal); Writing – original draft (supporting); Writing – review & editing (supporting). **Gregory A. Cooksey:** Conceptualization (equal); Data curation (supporting); Formal analysis (supporting); Funding acquisition (lead); Investigation (supporting); Methodology (equal); Project administration (lead); Resources (lead); Supervision (lead); Validation (equal); Visualization (equal); Writing – original draft (supporting); Writing – review & editing (supporting).

DATA AVAILABILITY

The data that support the findings of this study are available from the corresponding author upon request.

APPENDIX A: DERIVATION OF ANALYTICAL SOLUTION

Dividing Eq. (2) through by Q yields

$$\frac{1}{Q}\frac{\partial c}{\partial t} = -u(x,y)\frac{\partial c}{\partial z} - \xi\phi c\Theta(z). \tag{A1}$$

Shifting to a co-moving coordinate system recasts Eq. (A1) as an ODE. In particular, we define

$$\zeta = \frac{z}{u} + Qt, \tag{A2}$$

$$\omega = \frac{z}{u} - Qt, \tag{A3}$$

and note that

$$\frac{\partial}{\partial t} = \frac{\partial \zeta}{\partial t}\frac{\partial}{\partial \zeta} + \frac{\partial \omega}{\partial t}\frac{\partial}{\partial \omega}, \tag{A4}$$

29 February 2024 14:37:48

$$\frac{\partial}{\partial z} = \frac{\partial \zeta}{\partial z}\frac{\partial}{\partial \zeta} + \frac{\partial \omega}{\partial z}\frac{\partial}{\partial \omega}. \tag{A5}$$

Substituting these into Eq. (A1) yields

$$2\frac{\partial c}{\partial \zeta} = -\xi\phi c\Theta(z). \tag{A6}$$

Next, substitute $z = u(\zeta + \omega)$ into Eq. (A6) and divide both sides by c to find

$$\frac{1}{c}\frac{\partial c}{\partial \zeta} = -\frac{\xi\phi}{2}\Theta(u(\zeta + \omega)). \tag{A7}$$

Letting $y = \log(c)$, we integrate both sides with respect to ζ to find

$$\frac{\partial y}{\partial \zeta} = -\frac{\xi\phi}{2}\Theta(u(\zeta + \omega)), \tag{A8}$$

$$y = -\frac{\xi\phi}{2}[\Theta(u(\zeta + \omega))(\omega + \zeta)] + g(\omega) - y_0, \tag{A9}$$

where $g(\omega)$ and y_0 are integration constants. We now return to our original coordinates and exponentiate both sides to obtain an expression for $c(x, y, z, t)$,

$$y = -\frac{\xi\phi}{2}\left[\Theta(z)\left(\frac{2z}{u}\right)\right] + g\left(\frac{z}{u} - Qt\right) - y_0, \tag{A10}$$

$$c = e^{y}, \tag{A11}$$

$$c = e^{-y_0}\exp\left[-\frac{\xi\phi z}{u}\Theta(z) + g\left(\frac{z}{u} - Qt\right)\right]. \tag{A12}$$

The initial condition $c(x, y, z, t = 0) = c_0$ implies

$$y_0 = -\log c_0, \tag{A13}$$

$$g\left(\frac{z}{u} - Qt\right) = \xi\phi\Theta\left(\frac{z}{u} - Qt\right)\left(\frac{z}{u} - Qt\right). \tag{A14}$$

Inserting these integration constants into Eq. (A12) yields the full expression for c,

$$c(x, y, z, t) = c_0\exp\left[-\frac{\xi\phi z}{u(x, y)}\Theta(z) + \xi\phi\Theta\left(\frac{z}{u(x, y)} - Qt\right)\left(\frac{z}{u(x, y)} - Qt\right)\right]. \tag{A15}$$

We can now write simple expressions for the concentration of unbleached fluorophores in the two different regimes defined by the Heaviside step functions. In particular, one finds

$$c(x, y, z, t) = \begin{cases} c_0\exp\left(-\dfrac{\xi\phi z}{u(x, y)}\right) & \text{if } z < u(x, y)Qt \\ c_0\exp(-\xi\phi Qt) & \text{if } z > u(x, y)Qt. \end{cases} \tag{A16}$$

APPENDIX B: PECLET NUMBERS

At very low flows, the effect of diffusion begins to be non-negligible. This can be characterized by the Peclet number, Pe. We have previously shown that the uncertainty in the measured flow rate scales as Pe^{-1}.[22] Thus, keeping Pe and $\mathrm{Pe}_{\mathrm{eff}}$ above 20 ensures that the uncertainty will be ≲5 %. The three Peclet numbers for the system being modeled in this work are

$$\mathrm{Pe}_x = \frac{Qw}{Dd\mathscr{L}}, \quad \mathrm{Pe}_y = \frac{Qd}{Dw\mathscr{L}}, \quad \text{and} \quad \mathrm{Pe}_z = \frac{Q\mathscr{L}}{Dwd}. \tag{B1}$$

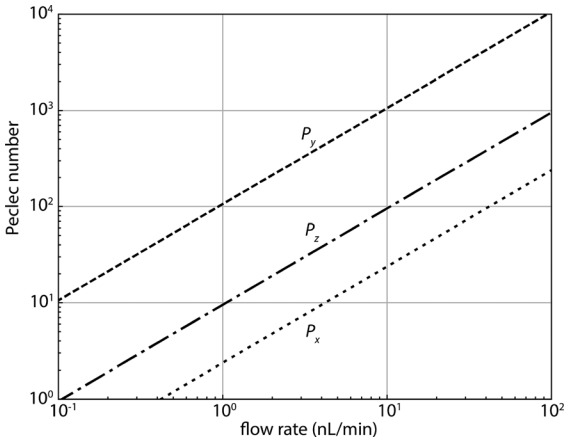

FIG. 6. The calculated Peclet numbers in each dimension as functions of the flow rate. The channel dimensions are taken to be a width of 15 μm, a depth of 100 μm, and an effective length (penetration depth) of 30 μm.

Figure 6 plots the three Peclet numbers as a function of flow rate. The flow channel dimensions of the flow meter used in this work are $d = 100$ μm, $w = 15$ μm, and $\mathscr{L} = 150$ μm, where d is the depth in the y-dimension, w is the width in the x-dimension, and $\mathscr{L}$ is the length in the z-dimension. However, the length of the illumination region is an overestimate of the relevant length-scale for determining the Peclet number. The length-scale we should use instead is the penetration depth of the fluorescence signal into the illumination region, i.e., the approximate width of the fluorescent spots seen in Fig. 1(c).[22] This effective length is dosage-dependent, so for the sake of simplicity, we take $\mathscr{L}_{\mathrm{eff}}$ to be 30 μm. We find that for flow rates of around 2 nl/min or less, $\mathrm{Pe}_z \lesssim 20$, and uncertainties due to diffusion begin to be non-negligible.

APPENDIX C: TIME CONSTANTS

There are at least three time constants relevant to this problem: (1) the time it takes liquid to traverse the interrogation region by advection, (2) the time it takes a fluorophore to diffuse across the interrogation region, and (3) the fluorophore bleaching time (Table II).

TABLE II. Relevant timescales for the flow rate. Approximate timescales were calculated using the values $A = w \times d = 15 \times 100$ μm^2, $L = 150$ μm, $L_{\mathrm{eff}} = 30$ μm, $Q = 0.5$ to 500 nl/min, $D = 3.5 \times 10^{-11}$ m^2/s, $P = 1$–100 mW, and $\phi = 10^{-13}$ J^{-1}.

Timescale	Expression	Approximate value
Advection	AL/Q	0.05–25 s
Diffusion	L_{eff}^2/D	25 s
Photobleaching	$1/P\phi$	0.2–20 s

29 February 2024 14:37:48

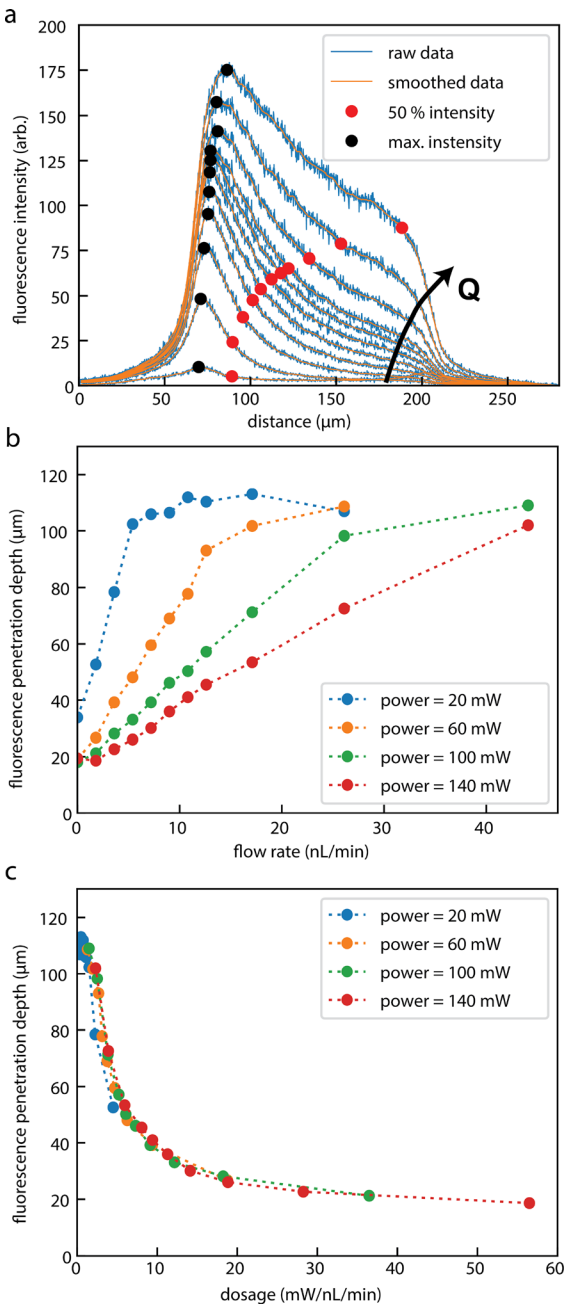

FIG. 7. (a) The fluorescence profile along the illumination region measured for ten different flow rates at 100 mW, measured by fluorescence microscopy. The black and red dots show the calculated position of maximum and half intensity, respectively, and the distance between these two points is taken to be the penetration depth. (b) The results of the penetration depth measurements shown in (a) repeated for four different powers. (c) The same data presented in (b) but plotted with dosage on the x-axis.

APPENDIX D: PENETRATION DEPTH

We measured the fluorescence penetration depth into the flow meter's illumination region for multiple values of flow rate and power. Figure 7(a) shows ten measurements preformed at flow rates of (0, 1.8, 3.6, 5.4, 7.2, 9.0, 10.8, 12.6, 17.1, and 26.1) nl/min, all at a laser power of 100 mW. The data were analyzed to estimate the penetration depth by finding the distance between the locations of maximum and half-maximum fluorescence intensity. It is apparent that the penetration depth increases with increasing flow rate. Figure 7(b) shows the results of four measurements taken at the same flow rates as Fig. 1(a) but at four different powers. For a fixed flow rate, the penetration depth is smaller with increasing power. This is to be expected from the predictions of Eq. (7), where the z-2dependence of the intensity profile for long times depends on $\exp(-\frac{\xi\phi z}{u})$. Figure 7(c) shows the same data as Fig. 6(b) but with dosage on the x-axis instead of the flow rate. All the curves collapse onto a single curve, demonstrating that the penetration depth is dosage-dependent. This means that the relationship between Peclet number and dosage is not simply linear as would be naively expected.

REFERENCES

[1]Z. Metaxiotou, H. Bissig, E. Batista, M. do Céu Ferreira, and A. Timmerman, "Metrology in health: Challenges and solutions in infusion therapy and diagnostics," Biomed. Eng./Biomed. Tech. **68**, 3–12 (2022).
[2]P. Lucas and S. Klein, "Metrology for drug delivery," Biomed. Eng./Biomed. Tech. **60**, 271–275 (2015).
[3]C. Mills, E. Batista, H. Bissig, F. Ogheard, A. W. Boudaoud, O. Büker, K. Stolt, J. Morgan, S. Kartmann, K. Thiemann *et al.*, "Calibration methods for flow rates down to 5 nl/min and validation methodology," Biomed. Eng./Biomed. Tech. **68**, 13–27 (2023).
[4]Z. Han and L. C. Chen, "A subtle change in nanoflow rate alters the ionization response as revealed by scanning voltage ESI-MS," Anal. Chem. **94**, 16015–16022 (2022).
[5]A. Schmidt, M. Karas, and T. Dülcks, "Effect of different solution flow rates on analyte ion signals in nano-ESI MS, or: When does ESI turn into nano-ESI?," J. Am. Soc. Mass Spectrom. **14**, 492–500 (2003).
[6]F. Zhou, Y. Lu, S. B. Ficarro, J. T. Webber, and J. A. Marto, "Nanoflow low pressure high peak capacity single dimension LC-MS/MS platform for high-throughput, in-depth analysis of mammalian proteomes," Anal. Chem. **84**, 5133–5139 (2012).
[7]K. Shoikhet and H. Engelhardt, "A photometric flow measurements method for characterisation of HPLC pumps," Chromatographia **38**, 421–430 (1994).
[8]O. Büker and K. Stolt, "Rise test facilities for the measurement of ultra-low flow rates and volumes with a focus on medical applications," Appl. Sci. **12**, 8332 (2022).
[9]E. Batista, N. Almeida, A. Furtado, E. Filipe, L. Sousa, R. Martins, P. Lucas, H. T. Petter, R. Snijder, and A. Timmerman, "Assessment of drug delivery devices," Biomed. Eng./Biomed. Tech. **60**, 347–357 (2015).
[10]EMPIR. "Report a1.2.5: Calibration methods for measuring the response or delay time of drug delivery devices using Newtonian liquids for flow rates from 5 nl/min to 100 nl/min." Technical Report (European Metrology Programme for Innovation and Research, 2022).
[11]E. Batista, A. Furtado, J. Pereira, M. Ferreira, H. Bissig, E. Graham, A. Niemann, A. Timmerman, J. Alves e Sousa, F. Ogheard *et al.*, "New EMPIR project—Metrology for drug delivery," Flow Meas. Instrum. **72**, 101716 (2020).
[12]E. Graham, K. Thiemann, S. Kartmann, E. Batista, H. Bissig, A. Niemann, A. W. Boudaoud, F. Ogheard, Y. Zhang, and M. Zagnoni, "Ultra-low flow rate measurement techniques," Meas.: Sens. **18**, 100279 (2021).
[13]A. Boudaoud, J. McGraw, T. Lopez-Leon, and F. Ogheard, "Traceability of the primary nano-flow measurement system: Measuring the local inner diameter of a glass capillary," Measurement **218**, 113141 (2023).
[14]M. Richter, P. Woias, and D. Wei*β*, "Microchannels for applications in liquid dosing and flow-rate measurement," Sens. Actuators, A **62**, 480–483 (1997).
[15]M. Ahrens, S. Klein, B. Nestler, and C. Damiani, "Design and uncertainty assessment of a setup for calibration of microfluidic devices down to 5 nl/min," Meas. Sci. Technol. **25**, 015301 (2014).

29 February 2024 14:37:48

[16]M. Ahrens, B. Nestler, S. Klein, P. Lucas, H. T. Petter, and C. Damiani, "An experimental setup for traceable measurement and calibration of liquid flow rates down to 5 nl/min," Biomed. Eng./Biomed. Tech. **60**, 337–345 (2015).
[17]H. Bissig, H. T. Petter, P. Lucas, E. Batista, E. Filipe, N. Almeida, L. F. Ribeiro, J. Gala, R. Martins, B. Savanier *et al.*, "Primary standards for measuring flow rates from 100 nl/min to 1 ml/min–gravimetric principle," Biomed. Eng./Biomed. Tech. **60**, 301–316 (2015).
[18]J. D. Wright and J. W. Schmidt, "Reproducibility of liquid micro-flow measurements," in *Proceeding of the 18th International Flow Measurement Conference (FLOMEKO2019)* (IMEKO (International Measurement Confederation), 2019), pp. 26–28.
[19]C. Cavaniol, W. Cesar, S. Descroix, and J.-L. Viovy, "Flowmetering for microfluidics," Lab Chip **22**, 3603–3617 (2022).
[20]A. Etminan, Y. S. Muzychka, K. Pope, and B. Nyantekyi-Kwakye, "Flow visualization: State-of-the-art development of micro-particle image velocimetry," Meas. Sci. Technol. **33**, 092002 (2022).
[21]G. A. Cooksey, P. N. Patrone, J. R. Hands, S. E. Meek, and A. J. Kearsley, "Dynamic measurement of nanoflows: Realization of an optofluidic flow meter to the nanoliter-per-minute scale," Anal. Chem. **91**, 10713–10722 (2019).
[22]P. N. Patrone, G. Cooksey, and A. Kearsley, "Dynamic measurement of nanoflows: Analysis and theory of an optofluidic flowmeter," Phys. Rev. Appl. **11**, 034025 (2019).
[23]P. N. Patrone, A. Q. Li, G. A. Cooksey, and A. J. Kearsley, "Measuring microfluidic flow rates: Monotonicity, convexity, and uncertainty," Appl. Math. Lett. **112**, 106694 (2021).
[24]J. Sadeghi, P. N. Patrone, A. J. Kearsley, and G. A. Cooksey, "Optofluidic flow meter for sub-nanoliter per minute flow measurements," J. Biomed. Opt. **27**, 017001 (2022).
[25]S. A. Soper, H. L. Nutter, R. A. Keller, L. M. Davis, and E. B. Shera, "The photophysical constants of several fluorescent dyes pertaining to ultrasensitive fluorescence spectroscopy," Photochem. Photobiol. **57**, 972–977 (1993).
[26]C. Eggeling, J. Widengren, R. Rigler, and C. A. Seidel, "Photobleaching of fluorescent dyes under conditions used for single-molecule detection: Evidence of two-step photolysis," Anal. Chem. **70**, 2651–2659 (1998).
[27]L. Song, E. Hennink, I. Young, and H. Tanke, "Photobleaching kinetics of fluorescein in quantitative fluorescence microscopy," Biophys. J. **68**, 2588–2600 (1995).
[28]A. P. Demchenko, "Photobleaching of organic fluorophores: Quantitative characterization, mechanisms, protection," Methods Appl. Fluoresc. **8**, 022001 (2020).
[29]P. R. Bevington, D. K. Robinson, J. M. Blair, A. J. Mallinckrodt, and S. McKay, "Data reduction and error analysis for the physical sciences," Comput. Phys. **7**, 415–416 (1993).
[30]G. H. Patterson and D. W. Piston, "Photobleaching in two-photon excitation microscopy," Biophys. J. **78**, 2159–2162 (2000).

29 February 2024 14:37:48